ROYAL SOCIETY OF CHEMISTRY

PAPER

Check for updates

Crystal structure, magnetic and magnetocaloric properties of the new orthorhombic Y₃Co₂-type Gd₃Co₁₊ₓNi₁₋ₓ solid solution†

Aritz Herrero, (ID) *[a] Alessia Provino,[bcd] Ivan R. Aseguinolaza,[a] Serena De Negri, (ID) [b] Davide Peddis, (ID) [be] Pietro Manfrinetti[bc] and Alberto Oleaga[a]

This work reports the existence of the new rare-earth intermetallic compound Gd₃Co₁₊ₓNi₁₋ₓ (with x = 0.1, 0.2, 0.3, and 0.4) and the investigation of its crystallographic, magnetic, and magnetocaloric properties. Gd₃Co₁₊ₓNi₁₋ₓ is a novel solid solution phase that crystallizes in the orthorhombic Y₃Co₂-type structure [$oP20$, *Pnmm* (no. 58)]. It constitutes the first representative of a compound crystallizing in this structural prototype. The research also includes an analysis of the critical behavior associated with the second-order phase transition from a paramagnetic to a ferromagnetic state (PM–FM) detected in the compound. This analysis indicates that short-range order isotropic magnetic interactions are present, consistent with the 3D Heisenberg model. Increasing the Co content leads to a higher Curie temperature (T_C), thus, shifting the peak of the magnetic entropy change, while maintaining the overall physical properties. This demonstrates the potential of tuning the working temperature region by modifying the Co/Ni concentration without negatively affecting the magnetocaloric properties. For $\mu_0\Delta H$ = 5 T, the magnetic entropy change peaks range between 7.81 and 8.40 J kg⁻¹ K⁻¹, while the refrigerant capacity values are around 600 J kg⁻¹. These results place this family among the top performing ones in their working temperature region. The scaling relations and the universal curve confirm the second-order nature of the phase transition and validate the calculated critical exponents.

1. Introduction

Reducing energy consumption, increasing the efficiency of heating and cooling devices, implementing new renewable energy sources and moving towards a greener economy and society are on the core of the current international scientific programs and research plans.[1–4] The effort towards the achievement of these goals is increasing year by year, with the research on new, more efficient and environmentally friendly refrigeration devices as one

of the most active research lines. To this end, magnetocaloric refrigeration has emerged as a promising candidate to fulfill the requirements of future energy demands. Besides the necessity of designing, building and testing the current refrigeration devices, the discovery of new magnetocaloric materials, the study of their crystallographic, thermal, magnetic and magnetocaloric properties, as well as the understanding of the physics ruling those properties, are the key to find the perfect magnetic refrigerant. To that end, many researchers are focusing their efforts on rare-earth based intermetallic compounds.[5,6] The interplay between rare-earth elements and the rest of the constituents usually gives rise to relevant magnetocaloric effects in a wide range of temperatures. This phenomenon is behind the growing interest in the synthesis and study of new intermetallic compounds. In particular, the ability to tune the physical properties of these compounds by slightly varying their composition, *i.e.* mixing rare-earth elements,[7–13] or substituting transition metals and/or p-block elements,[11,14–18] is of great interest. This allows a better understanding of the role of each constituent element in the final properties.

The present study aims to broaden the knowledge about a particular family of intermetallic compounds, R₃CoNi (R = rare earth element), for which few studies have been performed so far.[19–22] More specifically, this research is focused on the study

a Departamento de Física Aplicada, Escuela de Ingeniería de Bilbao, Universidad del País Vasco UPV/EHU, Plaza Torres Quevedo 1, 48013 Bilbao, Spain. E-mail: aritz.herrero@ehu.eus

b Department of Chemistry, University of Genova, Via Dodecaneso 31, 16146 Genova, Italy

c CNR, Institute SPIN, Corso Perrone 24, 16152 Genova, Italy

d Department of Material Sciences and Engineering, Alfred University, Alfred, New York 14802, USA

e CNR, Institute of Structure of Matter, nM2-lab, Monterotondo Scalo (RM), 00015, Italy

† Electronic supplementary information (ESI) available: Supplementary information to this article containing X-ray powder patterns, isothermal magnetization loops, critical behavior analysis, magnetocaloric scaling relations, universal curves and additional crystallographic data can be found online at the end of the document (DOC). See DOI: https://doi.org/10.1039/d5tc00423c

This journal is © The Royal Society of Chemistry 2025

J. Mater. Chem. C, 2025, **13**, 9027–9041 | **9027**

of the effect of Co/Ni substitution on the crystallographic, magnetic and magnetocaloric properties of the $Gd_3Co_{1+x}Ni_{1-x}$ family, with x = 0.1, 0.2, 0.3 and 0.4. Aiming to better understand the underlying physics of the system, the work will also include a critical behavior study of the second-order phase transition of the system from the paramagnetic state to the ferromagnetic state (PM–FM), which will provide insights into the range of magnetic interactions as well as the symmetry of the system. Unlike Ni, Co does not form a binary 'R₃Co₂' compound. Substitution of Ni by Co in the binary R_3Ni_2 phase, leading to the formation of $R_3Co_yNi_{2-y}$ phase, has been studied for R = Tb[21] and Gd,[22] with Co content $y \leq 1$ (lower than that of Ni and up to R₃CoNi composition). In contrast, the present investigation focuses on the opposite case, when Co content exceeds that of Ni. These previous studies have shown that in both $Gd_3Co_yNi_{2-y}$ and $Tb_3Co_yNi_{2-y}$ series,[21,22] an increase in the Co content consistently results in a higher Curie temperature (T_C). Therefore, we aimed to study the phase formation for Co rich compositions, to determine whether further tuning of the working temperature of these materials was possible while maintaining good magnetocaloric properties.

The new $Gd_3Co_{1+x}Ni_{1-x}$ compound was recently identified during a previous investigation of the binary Gd_3Ni_2 and its solid solution $Gd_3Co_yNi_{2-y}$ series (for $y \leq 1$).[22] Gd_3Ni_2 is a high temperature compound existing between 650 °C and 715 °C; this phase can be retained at room temperature by quenching (as a metastable phase). Interestingly, the partial substitution of Ni by Co to form $Gd_3Co_yNi_{2-y}$ stabilizes this solid-solution phase down to room temperature. Both Gd_3Ni_2 and the pseudobinary $Gd_3Co_yNi_{2-y}$ series crystallize in the monoclinic Dy₃Ni₂-type structure {Pearson symbol $mS20$, space group $C2/m$ (no. 12), $Z = 4$[23]}. This monoclinic structure is maintained up to Gd₃CoNi (for the Co content y = 1.0). Furthermore, it was ascertained that the crystal structure of Gd₃CoNi is a ternary ordered derivative of the monoclinic Dy₃Ni₂-type, where Co atoms preferentially occupy only one of the two 4i Wyckoff sites available for the transition metal.[22] Upon a further increase of the Co content beyond Gd₃CoNi (i.e. for $y > 1$), the crystal structure changes from the monoclinic Dy₃Ni₂-type to the orthorhombic Y₃Co₂-type [$oP20$, $Pnnm$ (no. 58), $Z = 4$][24] forming the new $Gd_3Co_{1+x}Ni_{1-x}$ compound. Notably, while the monoclinic Dy₃Ni₂-type structure is commonly adopted by several R₃Ni₂ and R₃CoNi intermetallic compounds,[19–21] the orthorhombic Y₃Co₂-type structure had only been reported for the prototype itself; no other binary or ternary compound has ever been reported to adopt this structure.[25] $Gd_3Co_{1+x}Ni_{1-x}$ is thus the first compound found to crystallize in the Y₃Co₂-type structure.[1] A crystallographic phase transition was also observed in the Tb₃Co_yNi₂₋_y series; however, in this case, increasing the Co content beyond $y \approx 0.34$ induces a structural change from the monoclinic Dy₃Ni₂-type to the rhombohedral Er₃Ni₂-type.[21]

In this work we report on the crystal structure of the new solid-solution $Gd_3Co_{1+x}Ni_{1-x}$ compound, present and discuss the magnetic and magnetocaloric properties along this series as a function of Co content (for x = 0.1, 0.2, 0.3, 0.4), and compare its physical properties with those observed in the monoclinic $Gd_3Co_yNi_{2-y}$ series ($y \leq 1$). Finally, we analyze the critical behavior associated with the second-order phase transition detected in this series, occurring from a paramagnetic to a ferromagnetic state.

2. Experimental section

2.1. Synthesis

Polycrystalline samples (each approximately 4 g in total mass), with the nominal composition $Gd_3Co_{1+x}Ni_{1-x}$, with x = 0.1, 0.2, 0.3, 0.4, were synthesized by arc melting the elements, weighed in stoichiometric proportion and under a pure Ar atmosphere. The starting constituents were high-purity commercial elements (Gd >99.9 wt% purity, Co and Ni, both 99.99 wt% purity); a slight excess of Gd (2 wt%) was added to prevent the possible formation of the equiatomic phase $GdCo_xNi_{1-x}$, which is ferromagnetic.[26] The buttons were melted three times, flipping them over between each melting to ensure homogeneity. Weight loss after melting was lower than 0.5% (about 0.2%). To maintain a clean atmosphere within the arc furnace, a TiZr getter was melted before melting each sample. The ingots were then wrapped in Ta foil, sealed under vacuum in quartz tubes, and annealed at 650 °C for 8 days (based on differential thermal analysis data). After annealing, the samples were slowly cooled to room temperature inside the furnace by simply switching off the power. The final samples exhibited typical metallic luster and brittle consistency.

2.2. Phase analysis

Phase analysis was conducted using scanning electron microscopy (SEM) coupled with energy dispersive X-ray spectroscopy (EDX) for semi-quantitative analysis, as well as X-ray diffraction (XRD) on both powder (PXRD) and single crystal (SCXRD) samples. The microstructure and homogeneity of the alloys were examined by SEM-EDX using a Leica Cambridge 360 microscope, equipped with an Oxford X-Max 20 analyzer. The operating parameters included an electron high tension (EHT) of 20.0 kV and a probe current of 220 pA, controlled through Oxford Aztec software; Co was used as an internal standard. Micrographic specimens were prepared by a standard polishing technique on a representative vertical section of each sample, cut from top to bottom. Since the weight loss of each sample during melting was negligible, the EDX analysis over the entire area of each specimen (15–20 mm²) was used as a reference standard of known composition to ensure the accuracy of the compositional analysis. This approach allowed for an estimated measurement accuracy within 0.5 at% for all elements.

2.3. Crystal structure determination

The crystal structure was determined by means of both powder and single-crystal X-ray diffraction. Powder diffraction patterns were collected with a Philips diffractometer (Cu K_α radiation, λ = 1.54184 Å) equipped with a line-detector. The powders were prepared by grinding polycrystalline pieces of each alloy and placing them on a zero-background Si-single-crystal sample

9028 | J. Mater. Chem. C, 2025, 13, 9027–9041

This journal is © The Royal Society of Chemistry 2025

holder. Data were collected over a 2θ range of 6–96°, with a step size of 0.02° and a counting time of 4–6 seconds per step. Pure Si [a = 5.4308(1) Å] was used as an internal standard. The X-ray powder patterns were indexed using Lazy Pulverix[27] and accurate lattice parameters were calculated using home-made least squares methods. The Rietveld refinement was performed for all four samples using the FullProf software.[28]

Single-crystal X-ray diffraction analysis was performed on a high-quality crystal selected from a crushed fragment of the sample with the nominal composition $Gd_3Co_{1.1}Ni_{0.9}$. The crystal was affixed to a glass fiber using grease and then loaded into the diffractometer. A complete dataset was collected under ambient conditions using a three-circle Bruker D8 QUEST diffractometer equipped with a PHOTON III detector (graphite monochromatized Mo K$_\alpha$ radiation, λ = 0.71073 Å) operating in ω-scan mode. Intensity data were collected over the reciprocal space up to $\approx$36.3° in θ (resolution of $\approx$0.6 Å), with exposures of 30 s per frame. The data were reduced and corrected for Lorentz, polarization, and absorption effects using APEX5.[29] The structure was solved and refined using the Bruker SHELXTL Software package.[30,31]

2.4. Magnetic measurements

Magnetization measurements were performed using a vibrating sample magnetometer (VSM) module installed in a physical properties measurement system (PPMS, Quantum Design). Various datasets were collected to thoroughly characterize the magnetism of the investigated compounds. The isofield magnetization, $M(T)$, was measured at a small applied magnetic field of 0.01 T between 2 K and 300 K and under zero-field-cooled (ZFC), field-cooled (FC) and field-warmed (FW) conditions. To study the magnetic behavior under varying applied magnetic field, isothermal magnetization curves, $M(H)$, were measured at temperatures ranging from 80 K to well above the Curie temperature. These measurements were performed under an externally applied magnetic field up to 7 T, using a step size of $\mu_0\Delta H$ = 0.1 T. Isotherms were collected at 5 K intervals, except near the magnetic phase transition at T_C where a finer temperature step of ΔT = 1 K was used to ensure accurate critical behavior analysis. For the purpose of correctly evaluating the magnetic entropy change, the demagnetization effect has been considered.[32] To this purpose, ac magnetic susceptibility measurements have been performed, from where the demagnetization factor (N) can be obtained using the Hopkinson maximum criteria.[33,34] After this, the internal magnetic field (H_i) is calculated following $H_i = H_a - NM$ (N being the demagnetization factor and H_a the applied magnetic field). To simplify the notation, H will be used from now on to denote the internal field H_i. The demagnetization factors obtained by this method for our compounds are 44.16 gOe emu^{-1} for x = 1.1, 39.06 gOe emu^{-1} for x = 1.2, 39.15 gOe emu^{-1} for x = 1.3 and 49.82 for x = 1.4.

Finally, in order to rule out the possibility of any kind of magnetic hysteresis, hysteresis loops at 2 K, 165 K and 225 K have been measured for every compound.

2.5. Resistivity measurements

The zero-field electrical resistivity was measured for $Gd_3Co_{1.1}Ni_{0.9}$ and $Gd_3Co_{1.4}No_{0.6}$ using the commercially available physical properties measurement system (PPMS, Quantum Design) on a home-made sample holder. The data were collected in a standard four-probe configuration, experimentally realised with Cu lids glued to the sample by silver paint, in a temperature range between 5 and 310 K.

3. Results and discussion

3.1. Crystal structure of $Gd_3Co_{1+x}Ni_{1-x}$

The crystal structure of $Gd_3Co_{1+x}Ni_{1-x}$ was initially identified from the powder X-ray diffraction pattern of an as-cast sample prepared with the nominal composition Gd_3CoNi, intended to synthesize the monoclinic Dy_3Ni_2-type Gd_3CoNi phase. In the X-ray powder pattern of this sample, together with the diffraction peaks of the monoclinic and primary phase, additional peaks were observed; these extra peaks were indexed to the primitive orthorhombic unit-cell of the Y_3Co_2 prototype structure.[22] The subsequent annealing process led to a sample with homogeneous composition, stabilizing the monoclinic phase as the unique equilibrium phase. Further investigation carried out in the present work revealed that the orthorhombic Y_3Co_2-type phase forms just as the Co content in the monoclinic Dy_3Ni_2-type $Gd_3Co_yNi_{2-y}$ exceeds y = 1.0. For this reason, we refer to the orthorhombic phase as $Gd_3Co_{1+x}Ni_{1-x}$.

The crystal structure of $Gd_3Co_{1+x}Ni_{1-x}$ was also confirmed by single-crystal X-ray diffraction on an annealed sample having the nominal composition $Gd_3Co_{1.1}Ni_{0.9}$. The structure was solved with the aid of the intrinsic phasing algorithm and refined using the Bruker SHELXTL Software package[30,31] in the space group *Pnnm* (with Z = 4 for the formula unit $Gd_3Co_{1.10}Ni_{0.90}$). The crystal data and structure refinement details are presented in Table S1 (ESI†). The corresponding CIF file, available as ESI,† has been deposited in the Cambridge Structural Database under deposition code CSD-2401455.

This structure features five inequivalent Wyckoff sites with $4g$ symmetry: three occupied by Gd atoms (occupied by Y in the prototype) and two occupied by Co or Co/Ni atoms (occupied by Co atoms in the prototype). Interestingly, the monoclinic structure of Gd_3Ni_2 and $Gd_3Co_yNi_{2-y}$ compounds, despite belonging to a different crystalline system, exhibits similar atomic arrangement with five inequivalent Wyckoff sites with $4i$ symmetry [three occupied by Gd atoms (Dy in the prototype) and two occupied by Co/Ni atoms (Ni in the prototype)].[22] Previous results from single-crystal X-ray diffraction and first-principles total energy calculations for the monoclinic Dy_3Ni_2-type Gd_3CoNi revealed crystallographic ordering, with a preferential occupation of Co atoms at the $4i$ site with coordinates (0.2378, 0, 0.2371) and Ni atoms at the $4i$ site with coordinates (0.0354, 0, 0.1425).[22] Based on these findings, the two $4g$ Wyckoff sites assigned to Co and Ni in the new orthorhombic $Gd_3Co_{1.1}Ni_{0.9}$ structure were carefully analyzed for possible Co/Ni preferential occupancy. Consistent with expectations,

This journal is © The Royal Society of Chemistry 2025

J. Mater. Chem. C, 2025, **13**, 9027–9041 | **9029**

Table 1 Standardized atomic coordinates, and isotropic (U_{eq}) and anisotropic (U_{ii}, U_{ij}, U_{jj}) displacement parameters for $Gd_3Co_{1.1}Ni_{0.9}$ (Y_3Co_2-type, $oP20$, $Pnmm$, no. 58) as obtained from single crystal analysis; $U_{23} = U_{13} = 0$

Atom	Wyckoff site	x/a	y/b	z/c	Occ.	U_{eq} [Å^2]
Gd_1	4g	0.43573(3)	0.36406(2)	0	1	0.01282(6)
Gd_2	4g	0.19030(3)	0.63045(2)	0	1	0.01402(7)
Gd_3	4g	0.62744(3)	0.10880(2)	0	1	0.01393(6)
Co	4g	0.13735(10)	0.23394(7)	0	1	0.01882(17)
Co/Ni	4g	0.12498(9)	0.03278(6)	0	0.1/0.9[a]	0.01806(15)

Atom	Wyckoff site	U_{11} [Å^2]	U_{22} [Å^2]	U_{33} [Å^2]	U_{23} [Å^2]	U_{13} [Å^2]	U_{12} [Å^2]
Gd_1	4g	0.01311(12)	0.01321(12)	0.01215(14)	0	0	−0.00029(9)
Gd_2	4g	0.01390(12)	0.01527(13)	0.01291(14)	0	0	−0.00081(9)
Gd_3	4g	0.01343(11)	0.01379(12)	0.01457(13)	0	0	−0.00039(10)
Co	4g	0.0297(4)	0.0148(3)	0.0120(4)	0	0	0.0004(3)
Co/Ni	4g	0.0198(3)	0.0170(3)	0.0174(4)	0	0	0.0003(3)

[a] Co/Ni occupancy was not refined.

a statistical analysis of multiple crystals revealed that the structural refinement converged with reasonably low and acceptable agreement factors only when the 4g site at coordinates (0.13735, 0.23394, 0) was fully occupied by Co atoms, and the 4g site at (0.12498, 0.03278, 0) was statistically filled by both Co and Ni with a 0.1 : 0.9 occupancy ratio, consistent with the nominal phase composition (confirmed by the EDX data) (Table 1).

The microstructure and the phase composition of the four samples were analyzed using SEM-EDX. The analyses revealed all samples to predominantly contain the orthorhombic $Gd_3Co_{1+x}Ni_{1-x}$ phase as the main phase, with small amounts of $Gd_3Co_{1-x}Ni_x$ (Fe_3Co-type, $oP16$, $Pnma$, no. 62) as the secondary phase. The SEM image showing the microstructure of the sample $Gd_3Co_{1.1}Ni_{0.9}$, chosen as a representative, is depicted in Fig. 1. Rietveld refinement was performed for all four samples
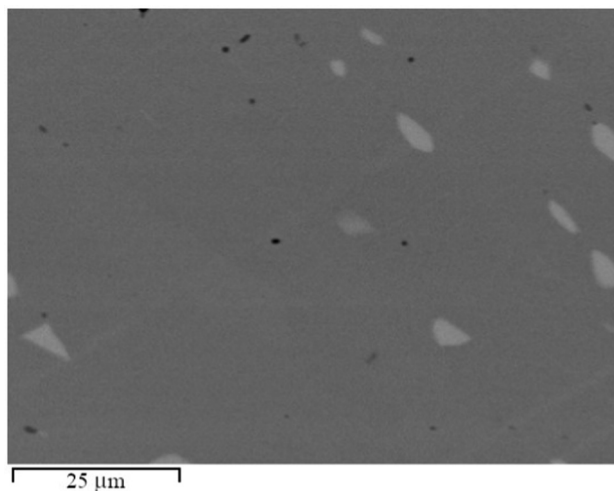

Fig. 1 SEM image (backscattered electron (BSE) mode) showing the microstructure of the $Gd_3Co_{1.1}Ni_{0.9}$ sample. The dark matrix corresponds to the new orthorhombic Y_3Co_2-type $Gd_3Co_{1.1}Ni_{0.9}$ phase and the light gray grains (trace of secondary phase) pertain to the $Gd_3Co_{1-x}Ni_x$ compound with x = 0.3 (Fe_3C-type). Note: the image refers to an area of the specimen richer in the extra phase.
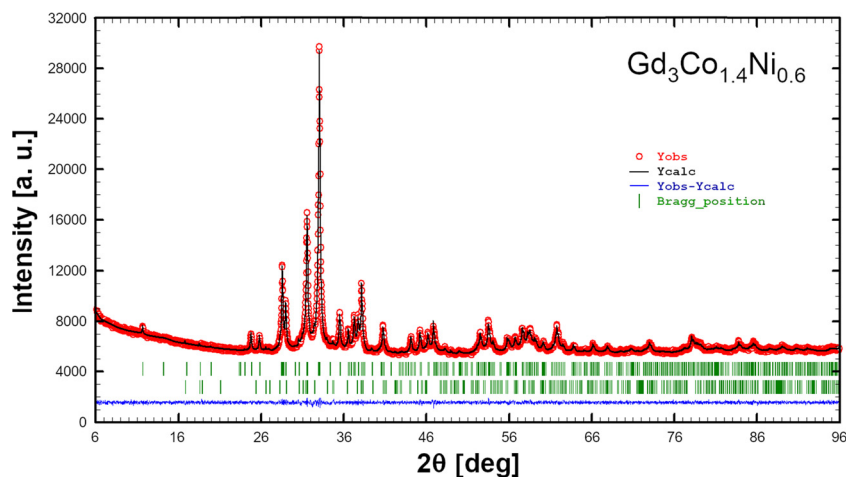
adopting the occupancies suggested by single-crystal data for the 4g sites assigned to Co and Ni, and accounting for the Co/Ni ratios measured by EDX [with Co occupying the 4g site at (0.13735, 0.23394, 0) and both Co and Ni occupying the 4g site at (0.12498, 0.03278, 0) in ratios 0.1 : 0.9, 0.2 : 0.8, 0.3 : 0.7 and 0.4 : 0.6]. The Co and Ni composition of both phases was kept constant and not refined during the Rietveld refinements.

By combining SEM-EDX with Rietveld refinement data, it was determined that the sample with nominal composition $Gd_3Co_{1.1}Ni_{0.9}$ contains ≈96 vol% $Gd_3Co_{1.10}Ni_{0.90}$ and ≈4 vol% $Gd_3Co_{1-x}Ni_x$ with x ≈ 0.3, the sample $Gd_3Co_{1.2}Ni_{0.8}$ contains ≈97 vol% $Gd_3Co_{1.20}Ni_{0.80}$ and ≈3 vol% $Gd_3Co_{1-x}Ni_x$ with x ≈ 0.3, the sample $Gd_3Co_{1.3}Ni_{0.7}$ contains ≈98.5 vol% $Gd_3Co_{1.30}Ni_{0.70}$ and ≈2.5 vol% $Gd_3Co_{1-x}Ni_x$ with x ≈ 0.2, and the sample $Gd_3Co_{1.40}Ni_{0.60}$ contains ≈98.2 vol% $Gd_3Co_{1.40}Ni_{0.60}$ and ≈1.8 vol% $Gd_3Co_{1-x}Ni_x$ with x ≈ 0.2. The Rietveld refinement profile for $Gd_3Co_{1.4}Ni_{0.6}$ is shown in Fig. 2, as an example. The corresponding profiles for the other three compounds are shown in Fig. S1–S3 (ESI†), while the relative atomic coordinates are reported in Tables S2–S5 (ESI†), respectively. Projections of the crystal structure along the three crystallographic axes are shown in Fig. 3. The coordination polyhedra in $Gd_3Co_{1.1}Ni_{0.9}$, pertaining to the first coordination sphere [this defined for $d_{obs}/\sum r_M \leq 1.166$, where d_{obs} is the observed interatomic distance between two next-neighbor atoms and $\sum r_M$ is the sum of the two metallic radii (where r_M = 1.802 Å, 1.252 Å and 1.246 Å for Gd, Co and Ni, respectively[35])], are shown in Fig. 4. The corresponding distances are provided in Table 2. Both the crystal structure and coordination polyhedra were drawn using VESTA software.[36] The coordination polyhedra surrounding Gd_1, Gd_2 and Gd_3 atoms are a 7-capped pentagonal prism, a 16-vertex Frank–Kasper polyhedron and a 14-vertex Frank–Kasper polyhedron, respectively, while the coordination polyhedra around Co and Co/Ni atoms are both tricapped trigonal prisms. The shortest interatomic distances in $Gd_3Co_{1.1}Ni_{0.9}$, as well as in the other members of the series $Gd_3Co_{1+x}Ni_{1-x}$ (up to x = 0.4), are those between Gd and Co (Gd−Co) and Co/Ni [Gd−(Co/Ni)] atoms (Table 2). As indicated by Rietveld refinement, these distances vary non-uniformly

9030 | J. Mater. Chem. C, 2025, **13**, 9027–9041

This journal is © The Royal Society of Chemistry 2025

Fig. 2 Observed X-ray powder pattern (red circle) and Rietveld refinement profile (black line) for the sample prepared on nominal composition $Gd_3Co_{1.40}Ni_{0.60}$. The lower profile (blue line) gives the difference between observed and calculated data; the Bragg angle positions are indicated by vertical bars (green). The sample contains ≈ 98 vol% of the new $Gd_3Co_{1.40}Ni_{0.60}$ compound (Y_3Co_2-type, $oP20$, $Pnnm$) (top Bragg angle bars) and ≈ 2 vol% of $Gd_3Co_{1-x}Ni_x$ ($x = 0.23$) (composition from EDX) (bottom Bragg angle bars).
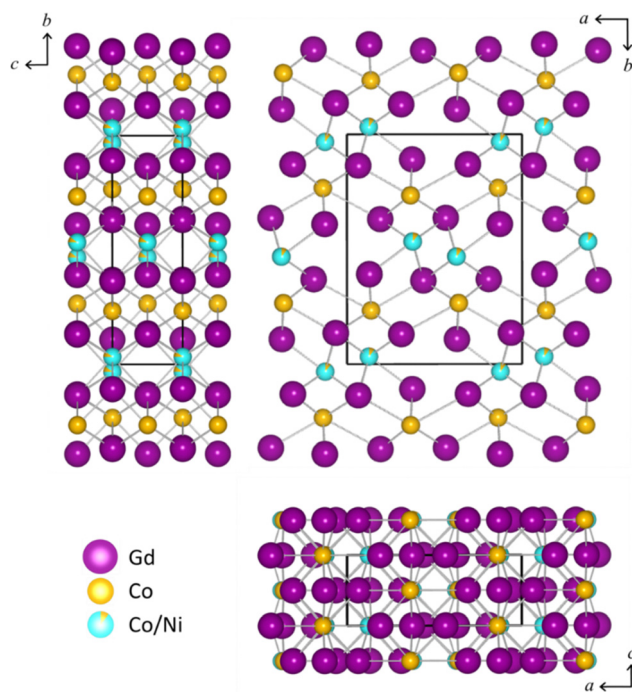

Fig. 3 Projections of the crystal structure of the orthorhombic Y_3Co_2-type $Gd_3Co_{1.1}Ni_{0.9}$ compound along the three crystallographic axes.
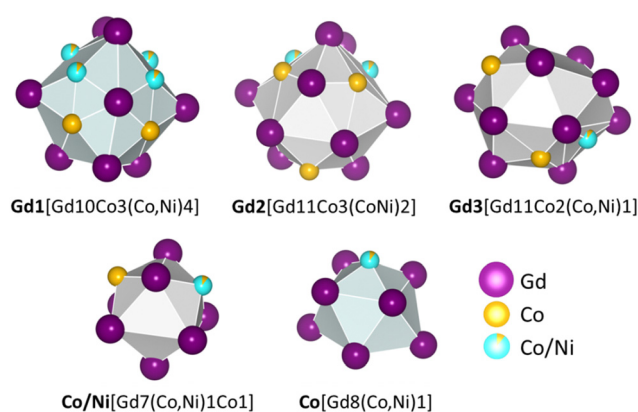

Fig. 4 Coordination polyhedra around Gd1, Gd2, Gd3, Co/Ni and Co atoms corresponding to the first coordination sphere for $d_{obs}/\sum r_M \leq 1.166$ in $Gd_3Co_{1.1}Ni_{0.9}$.

with increasing Co content. While all the Gd–(Co/Ni) distances decrease as the Co content increases, some Gd_1–Co and Gd_3–Co distances increase, and other Gd_1–Co, Gd_2–Co and Gd_3–Co distances decrease along the series. The specific values of interatomic distances obtained by Rietveld refinement for the four compounds are not reported to emphasize the qualitative analysis of the trends rather than numerical details.

The refined values of the lattice parameters (a, b, c) for the four $Gd_3Co_{1+x}Ni_{1-x}$ compounds are listed in Table 3, along with

the unit cell volume (V_{obs}), mean atomic volume (V_{at}), and volume of formation ($-\Delta V\%$), as well as the elemental composition measured by EDX for the orthorhombic phase and the one obtained considering a broad area (global area) of the sample, the so called global analysis. While the lattice parameters a and b decrease, the parameter c increases with increasing Co content (Fig. 5a). Consequently, both the unit cell volume and mean atomic volume decrease along the $Gd_3Co_{1+x}Ni_{1-x}$ series (Table 3). The trend of the unit cell volume as a function of x (Fig. 5b) is noteworthy. While the lattice parameters vary linearly with x, the unit cell volume follows a quadratic trend, decreasing and reaching a plateau at $x = 0.4$. This suggests that the $Gd_3Co_{1+x}Ni_{1-x}$ compound may not form for Co content exceeding ≈ 1.4/formula. Given that the atomic volume of elemental Co is slightly larger than that of Ni (11.08 Å^3 and 10.93 Å^3, respectively[37]), one would expect the opposite trend, *i.e.*, an increase of the unit cell volume with

This journal is © The Royal Society of Chemistry 2025

J. Mater. Chem. C, 2025, **13**, 9027–9041 | **9031**

Table 2 Interatomic distances corresponding to the first coordination sphere for $d_{obs}/\sum r_M \leq 1.166$ in $Gd_3Co_{1.1}Ni_{0.9}$, as obtained from single crystal analysis

Central atom	Ligands	d [Å]	$d_{obs}/\sum r_M$	Polyhedron
Gd_1	2 Co/Ni	2.9195(6)	0.957	7-Capped pentagonal prism $Gd[Gd_{10}Co_3(Co,Ni)_4]$
CN = 17	2 Co/Ni	2.9398(7)	0.964	
	2 Co	2.9866(7)	0.978	
	1 Co	3.2837(10)	0.911	
	2 Gd3	3.5326(3)	0.980	
	1 Gd2	3.5708(4)	0.991	
	1 Gd1	3.6271(4)	1.004	
	1 Gd3	3.6904(4)	1.024	
	2 Gd2	3.7081(3)	1.029	
	2 Gd1	3.8477(1)	1.068	
	1 Gd2	4.0834(4)	1.133	
Gd_2	2 Co	2.8454(7)	0.932	16-Vertex Frank–Kasper $Gd[Gd_{11}Co_3(CoNi)_2]$
CN = 16	2 Co/Ni	2.8835(7)	0.945	
	1 Co	3.5613(10)	1.166	
	1 Gd1	3.5708(4)	0.991	
	2 Gd3	3.6023(4)	1.000	
	2 Gd3	3.6170(3)	1.004	
	1 Gd3	3.7072(4)	1.029	
	2 Gd1	3.7081(3)	1.029	
	2 Gd2	3.8477(1)	1.067	
	1 Gd1	4.0834(4)	1.133	
Gd_3	2 Co	2.7583(7)	0.903	14-Vertex Frank–Kasper $Gd[Gd_{11}Co_2(Co,Ni)_1]$
CN = 14	1 Co/Ni	2.9573(9)	0.969	
	2 Gd1	3.5326(3)	0.980	
	2 Gd2	3.6023(4)	1.000	
	2 Gd2	3.6170(3)	1.004	
	1 Gd3	3.6584(4)	1.015	
	1 Gd1	3.6904(4)	1.024	
	1 Gd2	3.7072(4)	1.029	
	2 Gd3	3.8477(1)	1.068	
Co	1 Co/Ni	2.5282(12)	1.011	Tricapped trigonal prism $Co[Gd_8(Co,Ni)_1]$
CN = 9	2 Gd3	2.7583(7)	0.903	
	2 Gd2	2.8454(7)	0.932	
	2 Gd1	2.9866(7)	0.978	
	1 Gd1	3.2837(10)	1.075	
	1 Gd2	3.5613(10)	1.166	
Co/Ni	1 Co/Ni	2.5242(12)	1.010	Tricapped trigonal prism $(Co,Ni)[Gd_7(Co,Ni)_1Co_1]$
CN = 9	1 Co	2.5282(12)	1.011	
	2 Gd2	2.8835(7)	0.945	
	2 Gd1	2.9195(6)	0.957	
	2 Gd1	2.9398(7)	0.964	
	1 Gd3	2.9573(9)	0.969	

Table 3 Nominal composition, global EDX composition, EDX composition, lattice parameters (a, b, c), unit cell volume (V_{obs}), mean atomic volume (V_{at}) and volume of formation ($-\Delta V\%$) for the $Gd_3Co_{1+x}Ni_{1-x}$ compounds (x = 0.1, 0.2, 0.3, 0.4) (Y_3Co_2-type, $oP20$, $Pnmm$)

	Nominal composition			Global analysis from EDX			EDX composition of $Gd_3Co_{1+x}Ni_{1-x}$			Lattice parameters (Rietveld)					
Sample	Gd [at%]	Co [at%]	Ni [at%]	Gd [at%]	Co [at%]	Ni [at%]	Gd [at%]	Co [at%]	Ni [at%]	a [Å]	b [Å]	c [Å]	V_{obs} [Å³]	V_{at} [Å³]	$-\Delta V\%$
$Gd_3Co_{1.1}Ni_{0.9}$	60.00	22.00	18.00	60.97	22.20	16.83	60.65	22.03	17.32	9.54636(7)	12.5543(9)	3.85078(3)	461.510(6)	23.075	4.9026
$Gd_3Co_{1.2}Ni_{0.8}$	60.00	24.00	16.00	60.38	24.40	15.22	59.80	24.75	15.46	9.53984(5)	12.52853(7)	3.85994(2)	461.341(4)	23.067	4.9488
$Gd_3Co_{1.3}Ni_{0.7}$	60.00	26.00	14.00	60.81	25.35	13.83	59.96	26.01	14.04	9.53396(4)	12.50502(5)	3.86908(2)	461.280(3)	23.064	4.9728
$Gd_3Co_{1.4}Ni_{0.6}$	60.00	28.00	12.00	60.68	27.52	11.81	60.09	27.86	12.04	9.52957(7)	12.49058(8)	3.87524(2)	461.269(5)	23.063	4.9870

increasing Co content. A similar trend was observed in the monoclinic Dy_3Ni_2-type $Gd_3Co_xNi_{1-x}$ series,[22] further supporting the hypothesis of preferential site occupation by Co atoms in the Y_3Co_2-type $Gd_3Co_{1+x}Ni_{1-x}$ series.

By plotting both the unit cell volume and the volume of formation for both Dy_3Ni_2-type $Gd_3Co_xNi_{1-x}$ and Y_3Co_2-type $Gd_3Co_{1+x}Ni_{1-x}$ as a function of the Co content, x, two interesting trends are observed (Fig. 6a and b). The two trends indicate
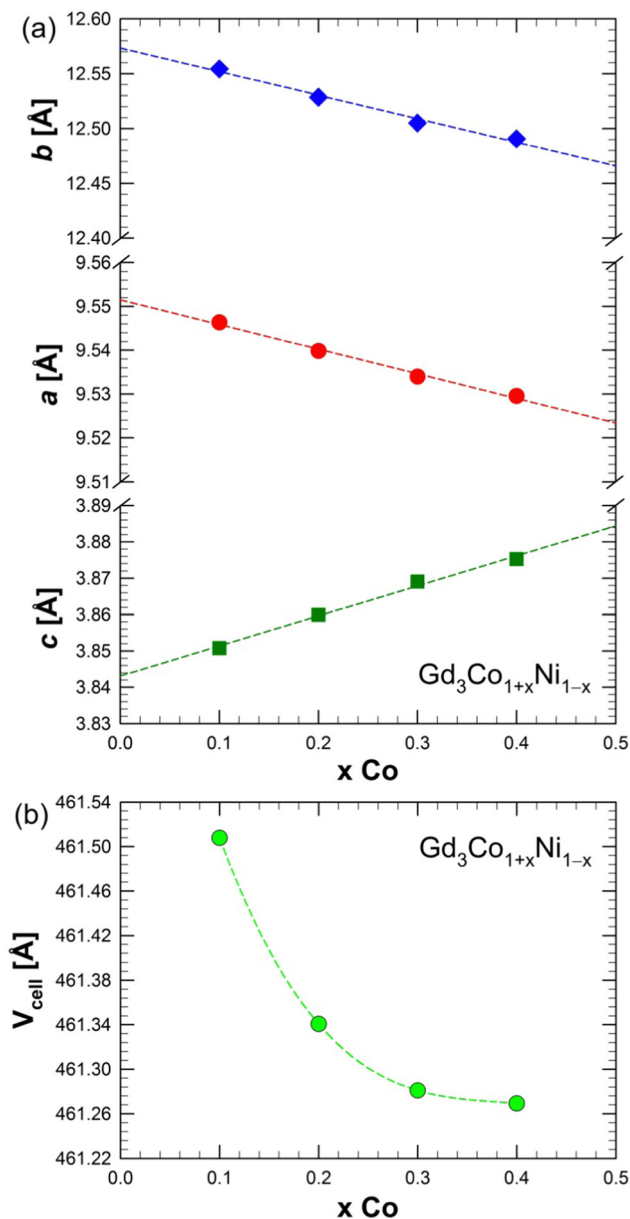
Fig. 5 Trend of the lattice parameters (a, b, c) (a) and unit cell volume (V_{cell}) (b) as a function of the Co content x in the orthorhombic Y_3Co_2-type $Gd_3Co_{1+x}Ni_{1-x}$ ($x = 0.1, 0.2, 0.3, 0.4$) series.

Fig. 6 Unit cell volume (V_{cell}) (a) and formation volume ($\Delta V\%$) (b) as a function of the Co content y in the monoclinic Dy_3Ni_2-type $Gd_3Co_yNi_{2-y}$ ($y = 0, 0.25, 0.50, 0.75, 0.85, 0.95, 1.00$) and in the orthorhombic Y_3Co_2-type $Gd_3Co_{1+x}Ni_{1-x}$ ($x = 0.1, 0.2, 0.3, 0.4$) compounds.

Dy_3Ni_2 and Y_3Co_2 prototypes are closely related to one another *via* displacements of slabs common to both structures, which is similar to the structural relationship between CrB-, FeB-, and TbNi-type structures.[24]

3.2. Physical properties

3.2.1. Electrical resistivity of $Gd_3Co_{1+x}Ni_{1-x}$. The electrical resistivity has been measured for $Gd_3Co_{1.1}Ni_{0.9}$ and $Gd_3Co_{1.4}Ni_{0.6}$ compounds, chosen as the representative of this series. The data are shown in Fig. 7. A typical metallic behavior, with the resistivity decreasing almost linearly with the temperature below 300 K, is observed. The resistivity data show a clear anomaly for both compounds, with a sharp change of slope in correspondence with the magnetic transition, as will be shown in the next section. Within the ordered state, the resistivity then decreases more rapidly with the freezing of spin-disorder scattering. The temperature at which the anomaly in the resistivity data occurs (about 182 K and 192 K for $Gd_3Co_{1.1}Ni_{0.9}$ and $Gd_3Co_{1.4}Ni_{0.6}$, respectively) is in good agreement with that observed in the magnetization data.

3.2.2. Magnetic properties. The ZFC magnetization data as a function of temperature, $M(T)$, collected at $\mu_0H = 0.01$ T and in

a common composition point [which is a maximum for V_{obs} *versus* x (Fig. 6a) and a minimum for $-\Delta V$ *versus* x (Fig. 6b)] occurring between $x = 0$ and $x = 1.1$, which is where the structural change occurs. The absolute values of the volume of formation ($|\Delta V|\%$) for the Y_3Co_2-type $Gd_3Co_{1+x}Ni_{1-x}$ phase range from 4.9% to 5.0%, while those for the Dy_3Ni_2-type $Gd_3Co_yNi_{2-y}$ compounds range from 4.7% to 5.1%. Although these two sets of values do not differ significantly from each other, their trend as a function of Co concentration is noteworthy for both phases. The new orthorhombic Y_3Co_2-type ($oP20$, $Pnnm$, no. 58, $Z = 4$) solid solution $Gd_3Co_{1+x}Ni_{1-x}$ represents a continuation of the monoclinic Dy_3Ni_2-type ($mS20$, $C2/m$, no. 12, $Z = 4$) solid solution $Gd_3Co_yNi_{2-y}$. The
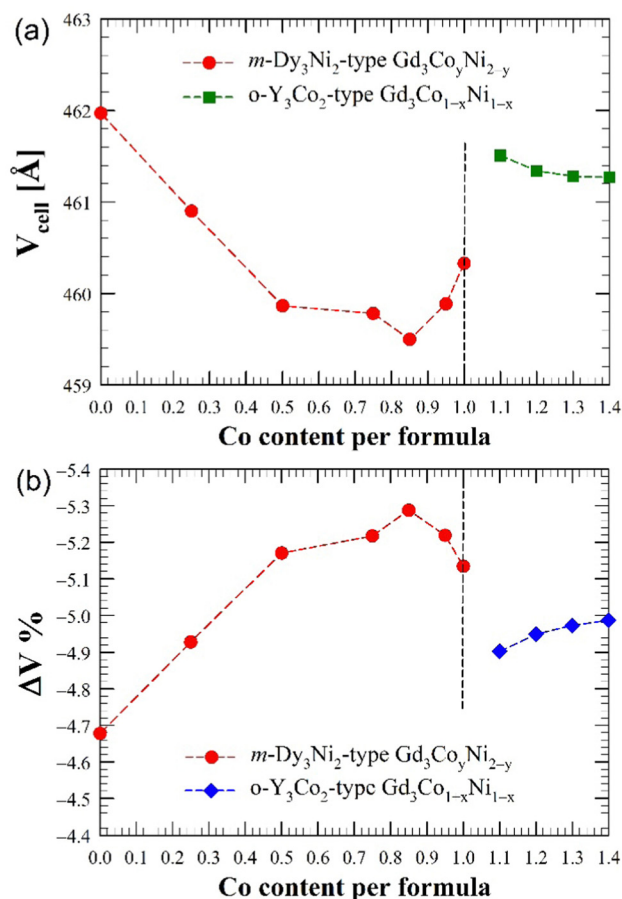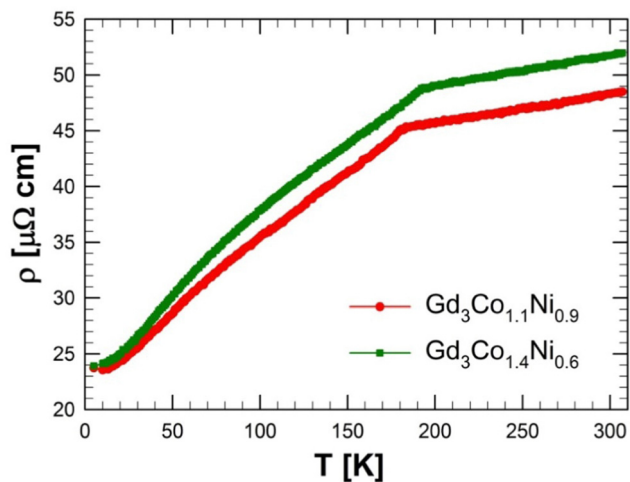
This journal is © The Royal Society of Chemistry 2025

J. Mater. Chem. C, 2025, **13**, 9027–9041 | **9033**

Fig. 7 Zero-field electrical resistivity for the $Gd_3Co_{1.1}Ni_{0.9}$ and $Gd_3Co_{1.4}Ni_{0.6}$ compounds as a function of temperature in the range of 5–300 K.

the range 2–300 K are shown in Fig. 8a for the four compounds. No significant difference was observed between ZFC, FC, and FW magnetization measurements. The isothermal magnetization, $M(H)$, at $T = 2$ K, 165 K and 225 K does not show hysteretic behavior (see the inset in Fig. 8a and Fig. S4 (ESI†)), as no measurable coercive fields have been found. This supports the second-order nature of the magnetic phase transitions, which was confirmed afterwards. The continuous increase in the Co/Ni ratio results on a monotonic increase of the Curie temperature, from $T_C \approx 177$ K for $GdCo_{1.1}Ni_{0.9}$ to $T_C \approx 186$ K for $GdCo_{1.4}Ni_{0.6}$. This trend suggests the possibility of tuning the T_C value for practical applications by controlling the Co/Ni concentration. This behavior agrees with the previously observed trend in the monoclinic Dy_3Ni_2-type $Gd_3Co_yNi_{2-y}$ $(0 \leq y \leq 1)$[22] and $Tb_3Co_yNi_{2-y}$ $(0 \leq y \leq 1)$.[21] However, if we compare our T_C data with those in ref. 22, we observe that the polynomial function proposed in the latter work for the T_C dependence on Co content can no longer be extrapolated to Co contents higher than Ni (see Fig. 8b). This discrepancy can

be ascribed to the different crystal structure adopted by the two series.

3.2.3. Critical behavior of the paramagnetic to ferromagnetic transitions. The next step in the comprehension of the magnetic interactions governing these systems is the careful study and analysis of the critical behavior of the PM to FM phase transition. It is well established, both theoretically and experimentally, that the critical behavior of some physical properties near second-order phase transitions can be characterized by certain critical exponents. This applies to the spontaneous magnetization (M_S), inverse of the initial susceptibility (χ_0^{-1}), and critical isotherm $M(H, T = T_C)$:[38]

$$M_S(T) \sim |t|^\beta \quad (T < T_C) \tag{1}$$

$$\chi_0^{-1}(T) \sim |t|^\gamma \quad (T > T_C) \tag{2}$$

$$M(H) \sim H^{1/\delta} \quad (T = T_C) \tag{3}$$

where $t = (T - T_C)/T_C$ is the reduced temperature, and β, γ and δ are the critical exponents. These exponents are universal, meaning that systems belonging to the same universal class are ruled by the same set of critical exponents, and, therefore, share some common properties such as the interaction extent, the dimension and the symmetry of the order parameter. The most common universality classes for magnetic materials are the well-known mean field ($\beta_{MF} = 0.5$, $\gamma_{MF} = 1$, $\delta_{MF} = 3$), 3D Heisenberg ($\beta_{Heis} = 0.3689(3)$, $\gamma_{Heis} = 1.3960(9)$, $\delta_{Heis} = 4.78$), and 3D Ising ($\beta_{Ising} = 0.32653(10)$, $\gamma_{Ising} = 1.2373(2)$, $\delta_{Ising} = 4.79$) models.[39–41]

Criticality can only be studied in second-order phase transitions; therefore, the first step is to confirm that the PM-to-FM transition is second order in all compounds. This has been verified by analysing the slopes of the magnetization isotherms represented in the so called Arrott plots, where M^2 is plotted as a function of H/M. According to the Banerjee criterion, if the slopes of all isotherms are positive, the transition corresponds to a second order, while if the slopes are negative, the transition is of first order.[42] As an example, Fig. 9a shows the Arrott plot
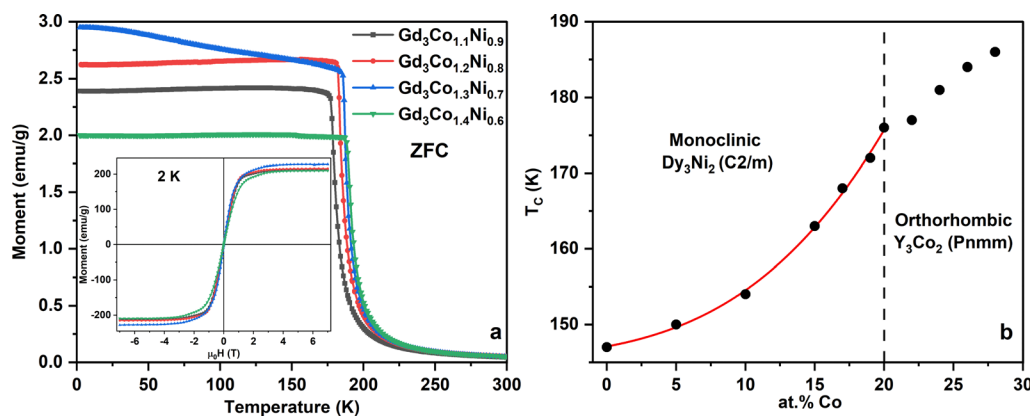

Fig. 8 ZFC magnetization at $\mu_0H = 0.01$ T for the four $Gd_3Co_{1+x}Ni_{1-x}$ (x = 0.1, 0.2, 0.3, 0.4) compounds (a); the inset shows the isothermal magnetization, $M(H)$, at $T = 2$ K. Variation of Curie temperature (T_C) as a function of the Co content (in at%) for both monoclinic Dy_3Ni_2-type $Gd_3Co_yNi_{2-y}$ and orthorhombic Y_3Co_2-type $Gd_3Co_{1+x}Ni_{1-x}$ (b).

9034 | *J. Mater. Chem. C*, 2025, **13**, 9027–9041
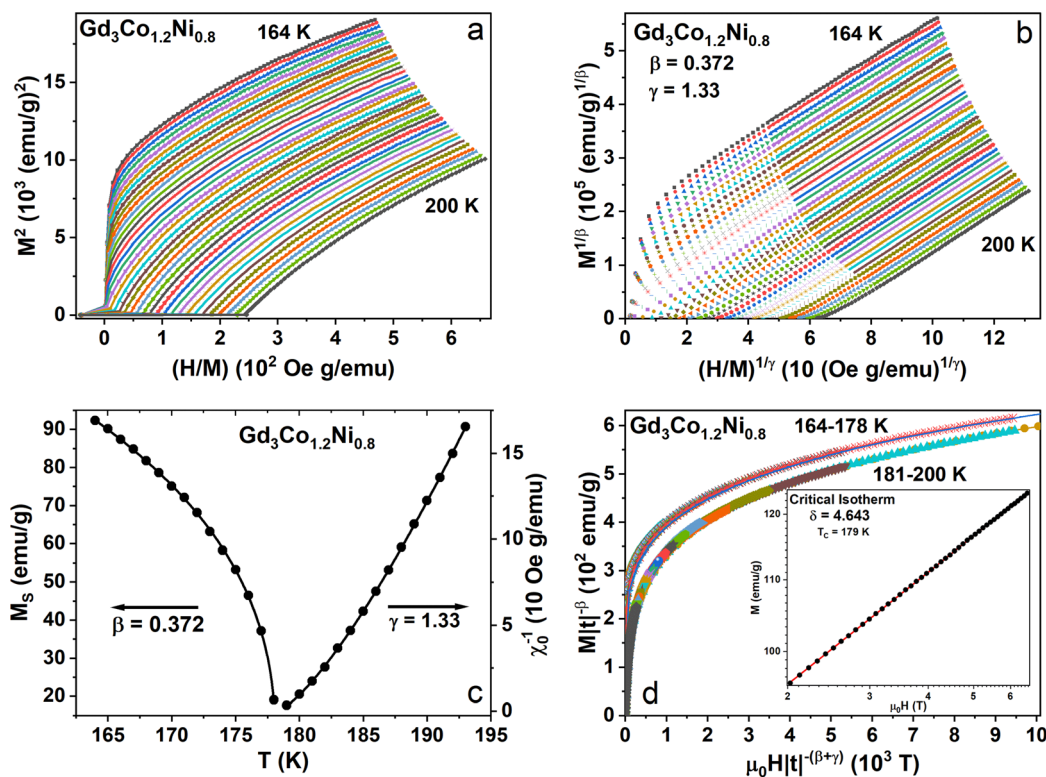
This journal is © The Royal Society of Chemistry 2025

Fig. 9 Critical behavior analysis for $Gd_3Co_{1.2}Ni_{0.8}$. Arrott plot representation (a); modified Arrott plot representation using the correct critical exponents (b); fitting of M_S and χ_0^{-1} to eqn (1) and (2) respectively (c); magnetic equation of state, with the inset showing the fitting of the critical isotherm to eqn (3) (d).

representation for $Gd_3Co_{1.2}Ni_{0.8}$, where it can be clearly seen that the slopes are positive, thus, confirming the second-order nature of the phase transition and the applicability of the critical behavior analysis. The same behavior is observed in every compound (see Fig. S5a, S6a and S7a in the ESI†). Once the order of the phase transition has been confirmed to be second order, a rigorous step-by-step iterative procedure is used in order to obtain the critical exponent. The process begins by representing the modified Arrott plots (MAPs), which consist in plotting $M^{1/\beta}$ as a function of $(H/M)^{1/\gamma}$. For the correct values of β and γ, the MAP should yield straight, parallel lines. Therefore, different universality models are tested in order to determine the best starting point. In this representation, the MF model corresponds with the Arrott plot, which clearly does not show the desired straight and parallel lines (see Fig. 9a). For every compound, the 3D Heisenberg model resulted in the best starting model. Once the starting model is chosen, M_S and χ_0^{-1} values are extracted from the interception of the straight lines in the MAP with the Y and X axes. These values are then fitted to eqn (1) and (2) to retrieve new values for β and γ. The critical exponents obtained through the previous fitting are then used to represent a new MAP, from where the process starts again until a convergence is reached. The final MAP for $Gd_3Co_{1.2}Ni_{0.8}$ can be seen in Fig. 9b as an example, and the corresponding final M_S and χ_0^{-1} fittings are shown in Fig. 9c. The β and γ critical exponent values obtained from the iterative method are listed in Table 4.

In order to assess the robustness of the critical exponents obtained from the previous iterative method, two further procedures are performed. The last critical exponent, δ, can be obtained from β and γ values using the Widom scaling equation:

$$\delta = 1 + \gamma/\beta \qquad (4)$$

The values of δ obtained from eqn (4) are listed in Table 4 as δ^*, and can be compared to the values of δ directly obtained from fitting the magnetization isotherm at the critical temperature to eqn (3), listed in the same table as δ. The values of δ obtained from both methods agree, supporting the results.

Table 4 Critical exponent values for the most common universality classes[39–41] and for the four compounds. δ^* values are calculated from the Widom scaling relation [eqn (4)], while δ values are obtained from the fittings of the critical isotherm following eqn (3)

	β	γ	δ	δ^*
Universality class				
Mean field	0.5	1	3	
3D Heisenberg	0.3689(3)	1.3960(9)	4.78	
3D Ising	0.32653(10)	1.2373(2)	4.79	
Compound				
$Gd_3Co_{1.1}Ni_{0.9}$	0.374 ± 0.005	1.34 ± 0.16	4.62 ± 0.01	4.58 ± 0.49
$Gd_3Co_{1.2}Ni_{0.8}$	0.372 ± 0.003	1.33 ± 0.02	4.643 ± 0.004	4.58 ± 0.07
$Gd_3Co_{1.3}Ni_{0.7}$	0.376 ± 0.003	1.29 ± 0.02	4.49 ± 0.008	4.44 ± 0.08
$Gd_3Co_{1.4}Ni_{0.6}$	0.387 ± 0.008	1.27 ± 0.05	4.302 ± 0.009	4.27 ± 0.21

This journal is © The Royal Society of Chemistry 2025

J. Mater. Chem. C, 2025, **13**, 9027–9041 | **9035**

The fitting of the critical isotherm for $Gd_3Co_{1.2}Ni_{0.8}$ is shown in the inset of Fig. 9d.

Finally, the reliability of the critical exponent values obtained has been confirmed by means of the magnetic equation of state, according to which the reduced magnetization $(M(H,t)|t|^{-\beta})$ should be a function of the reduced magnetic field $(f_{\pm}(H(t)|t|^{-(\beta+\gamma)})$:[38]

$$M(H,t)|t|^{-\beta} = f_{\pm}(H(t)|t|^{-(\beta+\gamma)}) \quad (5)$$

Here β and γ are the critical exponents and $\pm$ indicates a different function for isotherms above the critical temperature and below it. Therefore, if the correct critical exponents are used to represent the reduced magnetization as a function of the reduced magnetic field, the resulting graph should yield two distinct branches, one for each temperature region. An example of the magnetic equation of state can be seen for $Gd_3Co_{1.2}Ni_{0.8}$ in Fig. 9d, where the collapse of the isotherms into two branches is a clear indication of the reliability of the obtained values for the critical exponents. The plots for the other materials show exactly the same good agreement and they are shown in Fig. S5–S7 in the ESI.†

The critical exponents for the four compounds are close to the 3D Heisenberg model ($\beta_{Heis} = 0.3689(3)$, $\gamma_{Heis} = 1.3960(9)$, $\delta_{Heis} = 4.78$), which points to short-range order isotropic magnetic interactions. The β values of the two compounds with lower Co content ($Gd_3Co_{1.1}Ni_{0.9}$ and $Gd_3Co_{1.2}Ni_{0.8}$) agree, within the error, with the theoretical value corresponding to the 3D Heisenberg model. However, as the Co content increases, β slightly increases. A similar situation is found with the γ

critical exponent. The γ values for the compounds with the lowest Co content are close to the value corresponding to the 3D Heisenberg universality class, but, in this case, the value decreases as Co content increases. These deviations are common in Gd-based intermetallic compounds, for which the critical behavior studies of their PM–FM phase transitions also point to the 3D Heisenberg model.[43–45] This indicates that magnetism in these compounds mainly arises from Gd atoms; however, Co has been suggested to have a small magnetic moment in the Gd_3CoNi compound.[22] This magnetic moment may introduce magnetocrystalline anisotropy as the Co/Ni content increases, causing deviations of the critical exponents from the 3D Heisenberg universality class. A similar effect was observed in other members of this family when Gd was substituted by Nd in $Nd_xGd_{3-x}CoNi$.[20]

3.2.4. Magnetocaloric properties. The well-known Maxwell relation has been used to indirectly obtain the magnetic entropy change (ΔS_M) from the previously measured magnetic isotherms:

$$\Delta S_M(T, \Delta'H) = \mu_0 \int_{H_0}^{H_f} \left(\frac{\partial M}{\partial T}\right)_H dH \quad (6)$$

As an example, Fig. S8 (ESI†) shows the magnetization isotherms from which the magnetic entropy change has been calculated, along with the magnetization isofields for $Gd_3Co_{1.3}Ni_{0.7}$. The results obtained from using eqn (6) are shown in Fig. 10, where the magnetic entropy change for different applied magnetic field changes (ΔH) is represented as a function of temperature for the four compounds.
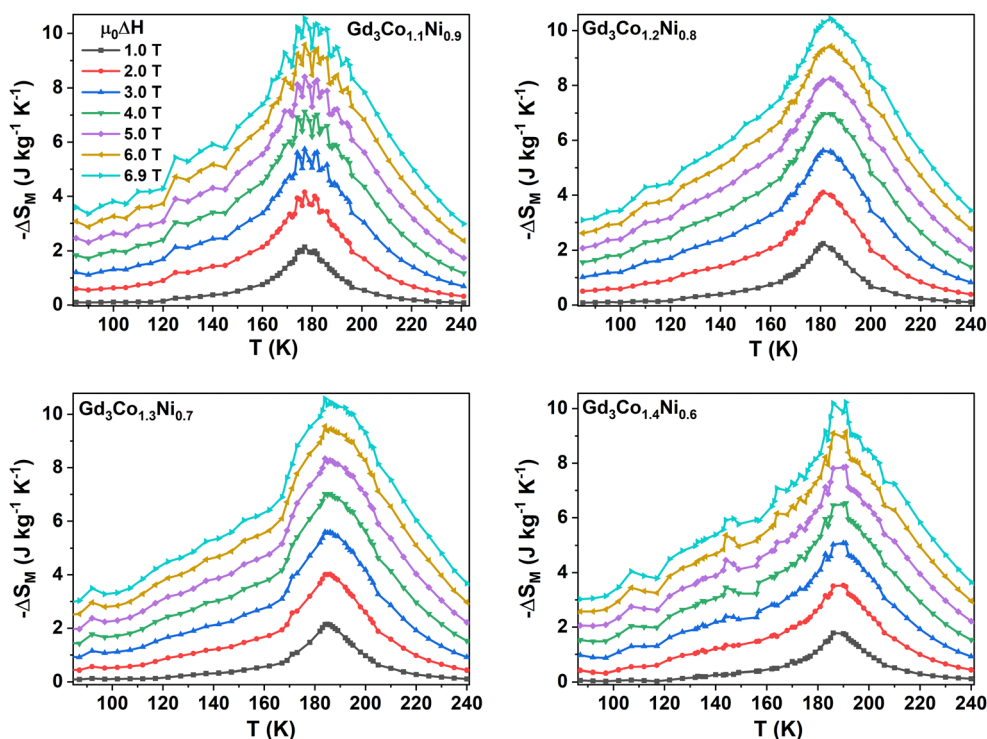

Fig. 10 Magnetic entropy change values for the different compounds at different $\mu_0\Delta H$ as a function of temperature. The legend is the same for all the graphs.

9036 | *J. Mater. Chem. C*, 2025, **13**, 9027–9041

This journal is © The Royal Society of Chemistry 2025

As expected, each sample shows a peak at its corresponding Curie temperature, where the magnetization change is most pronounced. The peak values of the magnetic entropy change ($|\Delta S_M^{pk}|$), for applied fields of $\mu_0 \Delta H$ = 2, 5 and 6.9 T (selected for comparison with the literature), are listed in Table 5. This table also contains further valuable information for assessing the applicability of these materials as magnetic refrigerants, such as the refrigerant capacity (RC), calculated using the two most common methods. The refrigerant capacity at full width at half maximum (RC$_{FWHM}$):

$$RC_{FWHM} = |\Delta S_M^{pk}|\delta T_{FWHM} \qquad (7)$$

where δT_{FWHM} is the temperature width of the peak at half the value of the peak, and RC$_{Area}$ defined as the area enclosed by the magnetic entropy change in δT_{FWHM}:

$$RC_{Area} = \int_{T_{cold}}^{T_{hot}} |\Delta S_M(T, \Delta H)|dT \qquad (8)$$

Finally, the temperature averaged entropy change TEC$_{10}$ defined as[46,47]

$$TEC_{10} = \frac{1}{10}\int_{T^{pk}-5}^{T^{pk}+5} \Delta S_M(T')dT' \qquad (9)$$

where T^{pk} is the temperature at which the peak is located, has also been evaluated.

The data in Table 5 show that the increase of Co content over Ni shifts the peak to higher temperatures. However, the magnetocaloric properties remain well preserved across all four compounds. This is interesting as it opens the possibility of tuning the transition temperature within a 10 K range without compromising the magnetocaloric properties. These values can be compared to those in ref. 22, where members of the same family with lower Co content [Gd$_3$Co$_y$Ni$_{2-y}$ ($0 \leq y \leq 1$)] were studied. In this latter study, $|\Delta S_M^{pk}(\mu_0 \Delta H = 5T)|$ slightly increases with Co content from 8.0 J kg^{-1} K^{-1} for Gd$_3$Ni$_2$ to 8.3 J kg^{-1} K^{-1} for Gd$_3$CoNi, while RC$_{FWHM}(\mu_0 \Delta H = 5T)$ values are approximately on the order of 540 J kg^{-1}. These values are similar to those obtained in this study, suggesting the possibility of further tuning the working temperature region from 147 K

(T_C of Gd$_3$Ni) to 186 K (T_C of Gd$_3$Co$_{1.4}$Ni$_{0.6}$), a shift of almost 40 K, solely by changing the Co/Ni concentration while preserving the good magnetocaloric properties. This contrasts with the behavior observed in Gd$_3$CoNi when Gd was partially substituted by Nd,[20] where an equal amount of Gd and Nd resulted in a drastic reduction of the magnetic entropy change peak at $\mu_0 \Delta H$ = 5 T to 4.1 J kg^{-1} K^{-1} (half the value of the parent compound Gd$_3$CoNi) and a drop of RC$_{FWHM}$ to one fifth of the values obtained in this work.

The magnetocaloric properties of these materials are outstanding when compared to other rare-earth containing compounds in the same working temperature region. In particular, the $|\Delta S_M^{pk}|$ values obtained in this work are higher than any other value (within the same temperature region) presented in Fig. 25 of ref. 48, an extensive review covering hundreds of magnetocaloric materials. This comparison can be extended to the equiatomic GdCo$_y$Ni$_{1-y}$,[26] with a slightly lower working temperature region ranging from 150 K for y = 0.5 to 171 K for y = 0.7. In GdCo$_y$Ni$_{1-y}$, the values of the magnetic entropy change peak at 5 T are very similar to those obtained in this work, with the lowest value, $|\Delta S_M^{pk}|$ = 8.2 J kg^{-1} K^{-1}, corresponding to the composition with y = 0.7 and the highest one, $|\Delta S_M^{pk}|$ = 9.7 J kg^{-1} K^{-1}, to y = 0.5. The RC$_{FWHM}$ values at 5 T obtained for the aforementioned compounds are also similar, though lower (between 508 and 574 J kg^{-1}) than those of the compositions presented in this work.

Some magnetocaloric properties, such as the magnetic entropy change peak $|\Delta S_M^{pk}|$ and the RC, are known to scale with the applied magnetic field according to the following relations:[49,50]

$$\Delta S_M^{pk} \sim H^{1+\left(\frac{1}{\delta}\right)\left(1-\frac{1}{\beta}\right)} = H^n \qquad (10)$$

and

$$RC \sim H^{1+1/\delta} \qquad (11)$$

where β and δ are the critical exponents which characterize the second order magnetic phase transition of the corresponding compound. These equations and the critical exponent values in Table 4 have been used to check the scaling of these magnetocaloric properties and further confirm the validity of the

Table 5 Magnetic entropy change peak, RC$_{FWHM}$, RC$_{Area}$ and TEC$_{10}$ values at $\mu_0 \Delta H$ = 2, 5 and 6.9 T for the four compounds

| | | Gd$_3$Co$_{1.1}$Ni$_{0.9}$ | Gd$_3$Co$_{1.2}$Ni$_{0.8}$ | Gd$_3$Co$_{1.3}$Ni$_{0.7}$ | Gd$_3$Co$_{1.4}$Ni$_{0.6}$ |
		T_C = 177 K	T_C = 181 K	T_C = 184 K	T_C = 186 K
2 T	$|\Delta S_M^{pk}|$ (J kg^{-1} K^{-1})	4.15	4.10	4.01	3.51
	RC$_{FWHM}$ (J kg^{-1})	154	166	157	150
	RC$_{Area}$ (J kg^{-1})	114	125	119	110
	TEC$_{10}$ (J kg^{-1} K^{-1})	3.76	3.80	3.71	3.25
5 T	$|\Delta S_M^{pk}|$ (J kg^{-1} K^{-1})	8.40	8.25	8.34	7.81
	RC$_{FWHM}$ (J kg^{-1})	618	640	572	628
	RC$_{Area}$ (J kg^{-1})	443	468	423	437
	TEC$_{10}$ (J kg^{-1} K^{-1})	7.88	8.03	7.98	7.37
6.9 T	$|\Delta S_M^{pk}|$ (J kg^{-1} K^{-1})	10.55	10.44	10.58	10.20
	RC$_{FWHM}$ (J kg^{-1})	994	976	913	931
	RC$_{Area}$ (J kg^{-1})	704	710	662	646
	TEC$_{10}$ (J kg^{-1} K^{-1})	9.89	10.17	10.16	9.59

This journal is © The Royal Society of Chemistry 2025

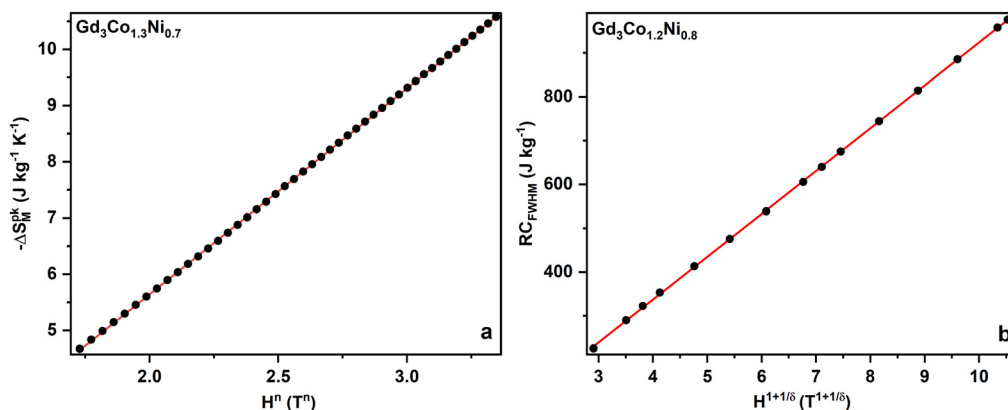*J. Mater. Chem. C*, 2025, **13**, 9027–9041 | 9037

Fig. 11 Field dependence of the magnetic entropy change peak for $Gd_3Co_{1.3}Ni_{0.7}$ (a) and RC_{FWHM} for $Gd_3Co_{1.2}Ni_{0.8}$ (b); the red line is a linear fit to be used as a visual guide.

obtained critical exponents. As an example, the results are shown in Fig. 11 for the magnetic entropy change at the peak value of $Gd_3Co_{1.3}Ni_{0.7}$ (a) and for RC_{FWHM} of $Gd_3Co_{1.2}Ni_{0.8}$ (b); the scaling for the other compounds is reported in Fig. S9 and S10 in the ESI.† The red line is a linear fit used as a visual reference. The good scaling obtained is proof of the validity of the scaling relations and the correct calculation of the corresponding critical exponents and subsequent analysis.

The temperature dependence of the exponent $n(T)$ defined in eqn (10) also provides valuable information about the system. In second-order phase transitions, $n(T)$ should vary monotonically, tending to a value of 2 in the paramagnetic phase as temperature increases and to $n(T)1$ in the ferromagnetic phase, with a minimum at T_C. However, an overshoot of the n parameter well above $n > 2$ would indicate a first-order transition.[47,51] As an example, the $n(T)$ curve at 7 T for $Gd_3Co_{1.4}Ni_{0.6}$ is presented in Fig. 12, where the usual behavior for second order phase transition is observed, with the absence

of any overshoot. The same behavior is found for the other three compounds (see Fig. S11 in the ESI†).

Another useful tool coming from the universality nature of second-order phase transitions is the so-called universal curve. Universality implies that all the magnetic entropy change curves corresponding to a certain compound should collapse into a single one after normalizing to the peak value of each curve ($\Delta S_M/\Delta S_M^{pk}$) and rescaling the temperature axis according to ref. 50 and 52:

$$\theta = (T - T_C)/(T_r - T_C) \tag{12}$$

Here T_C is the Curie temperature and T_r is the reference temperature corresponding to a particular fraction of $|\Delta S_M^{pk}|$, which is usually chosen as $\Delta S_M(T_r) = 0.5\Delta S_M^{pk}$. Fig. 13 shows an example of the overlapping of the different isofields onto a single curve in the case of $Gd_3Co_{1.1}Ni_{0.9}$. The universal curves for the other compounds can be seen in Fig. S12 (ESI†). The existence of this universality curve is a demonstration of the second-order nature of the phase transition. Furthermore, this curve, together with the scaling relation of ΔS_M^{pk}, enables the
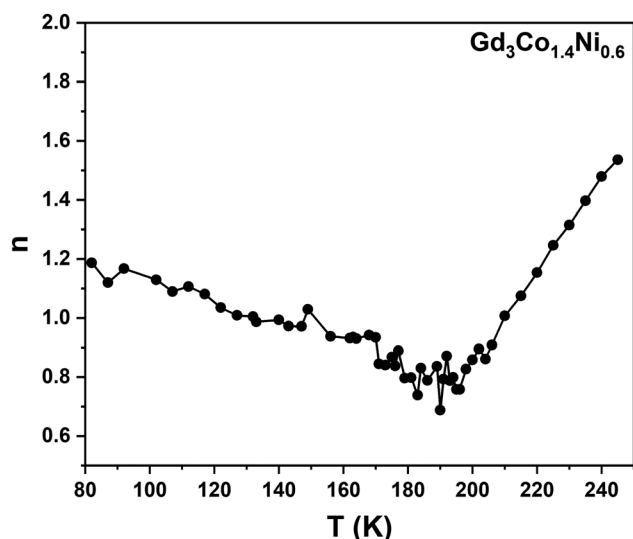

Fig. 12 Temperature dependence of the n exponent for $Gd_3Co_{1.4}Ni_{0.6}$ at 7 T.
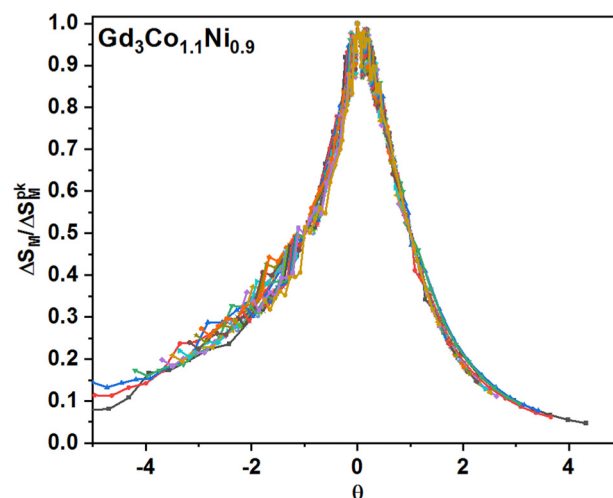

Fig. 13 Universal curve for the $Gd_3Co_{1.1}Ni_{0.9}$ compound.

extrapolation of the magnetocaloric properties to applied magnetic fields and temperatures beyond instrumental limitations.[53]

4. Conclusions

The present investigation provides a comprehensive analysis of the interplay between chemical composition, structural rearrangement and the resulting physical properties in the new orthorhombic $Gd_3(Co,Ni)_2$ (Y_3Co_2-type $Gd_3Co_{1+x}Ni_{1-x}$) compared with the monoclinic $Gd_3(Co,Ni)_2$ (Dy_3Ni_2-type $Gd_3Co_yNi_{2-y}$).[22] We observe that the structural change from the monoclinic Dy_3Ni_2-type to the orthorhombic Y_3Co_2-type, occurring when the Co/Ni content per formula unit exceeds >1, has significant implications for the material's magnetic and electronic behavior. X-ray diffraction confirms the orthorhombic Y_3Co_2-type structure for the $Gd_3Co_{1+x}Ni_{1-x}$ compounds to form when $x > 1$ and remain stable up to $x = 1.4$. It was also found that, between the two $4g$ Wyckoff sites occupied by the transition metal, one is exclusively occupied by Co atoms, while the other exhibits mixed occupancy of Co and Ni. This ordered arrangement aligns well with and follows the progressive preferential ordered Co/Ni distribution previously observed in the monoclinic Dy_3Ni_2-type $Gd_3Co_yNi_{2-y}$ compounds. Additionally, the unexpected decrease in the unit-cell volume with increasing Co content, accompanied by a non-uniform variation of the interatomic distances, suggests a complex interplay between the atomic properties (atomic size, valence and electronegativity) and site occupation. The study also analyses the evolution of the lattice parameters and unit-cell volume across the $Gd_3Co_{1+x}Ni_{1-x}$ series. It reveals that while the a and b lattice parameters decrease linearly with increasing Co content, parameter c increases. This trend leads to a quadratic decrease in the unit-cell volume, which reaches a plateau at $x = 0.4$ ($Gd_3Co_{1.4}Ni_{0.6}$), suggesting this Co concentration as the solubility limit of the orthorhombic phase.

The critical exponents for the $Gd_3Co_{1+x}Ni_{1-x}$ compounds ($x = 0.1, 0.2, 0.3,$ and 0.4) suggest short-range order isotropic magnetic interactions, aligning with the 3D Heisenberg model. As Co concentration increases, slight deviations from the 3D Heisenberg universality class emerge. These deviations may be due to the magnetocrystalline anisotropy induced by the possible Co magnetic moment. A similar effect has been observed in other compounds within this family when Nd partially substitutes Gd.[20]

Increasing the Co content over Ni leads to a higher Curie temperature, consistent with previous observations in the $Gd_3Co_xNi_{2-x}$ and $Tb_3Co_xNi_{2-x}$ series.[21,22] This results in a shift of the peak of the magnetic entropy change to higher temperatures with the increase of Co content, without negatively affecting the magnetocaloric properties. Comparing the results of this work to previous studies on the same family (with lower Co content)[22] reveals the possibility of precisely tuning the working temperature region from 147 K to 186 K by modifying the Co/Ni concentration.

The analysis of scaling relations and the universal curve confirms the second-order nature of the phase transition in the studied compounds and validates the accuracy of the calculated critical exponents.

The results demonstrate that tuning the Co/Ni concentration allows for precise control of the working temperature range for magnetocaloric applications, potentially making these materials suitable for efficient and sustainable cooling technologies.

Data availability

The data supporting this article have been included and discussed as part of the manuscript. The data obtained from the relative measurements performed in this study, and the data from which the resulting results were derived/extracted, are original and already provided in the several different tables in the manuscript. Further, the crystal data and structure refinement details of the compound $Gd_3Co_{1.1}Ni_{0.9}$ (which are presented in Table 1) are fully available as a CIF file deposited in the Cambridge Structural Database center by citing the deposition code CSD-2401455. Complementary information mentioned in the manuscript is available in the ESI.† For other datasets associated with previous studies, data citations in the proper format are included in the article.

Conflicts of interest

There are no conflicts to declare.

Acknowledgements

References

1 Agenda 21: programme of action for sustainable development, Rio declaration on environment and development, statement of forest principles: the final text of agreements negotiated by Governments at the United Nations Conference on Environment and Development (UNCED), 3–14 June 1992, Rio de Janeiro, Brazil, 1993, 294, **https://sustainabledevelopment.un.org/outcomedocuments/agenda21**.

2 Enerdata, Global Energy Trends – 2021 Edition (2021), **https://www.enerdata.net/publications/reports-presentations/2021-energy-climate-trends.html**.

3 U. S. Environmental Protection Agency, Climate Change Indicators: Residential Energy Use (EPA, 2021), **https://www.epa.gov/climate-indicators/climate-change-indicators-residential-energy-use**.

4 IEA, The Future of Cooling (IEA, Paris, 2018), **https://www.iea.org/reports/the-future-of-cooling**.

This journal is © The Royal Society of Chemistry 2025

J. Mater. Chem. C, 2025, **13**, 9027–9041 | **9039**

5 W. Liu, T. Gottschall, F. Scheibel, E. Bykov, A. Aubert, N. Fortunato, B. Beckmann, A. M. Doring, H. Zhang, K. Skokov and O. Gutfleisch, A matter of performance and criticality: A review of rare-earth-based magnetocaloric intermetallic compounds for hydrogen liquefaction, *J. Alloys Compd.*, 2024, **995**, 174612.

6 J. Y. Law and V. Franco, Modern rare-earth-containing magnetocaloric materials: Standing on the shoulders of giant Gd$_5$Si$_2$Ge$_2$, *Handbook on the Physics and Chemistry of Rare Earths*, 2023, ch. 332, vol. 64, pp. 175–246.

7 B. Hilliard, V. S. R. de Sousa, K. Dixon-Anderson, Y. Mudryk and J. Cui, Magnetocaloric effect in Gd$_{1-x}$Ce$_x$Ni ($x = 0$–0.6): A cost-effective approach to tuning Curie temperature from 70 K to 30 K, *J. Alloys Compd.*, 2024, **989**, 174186.

8 D. Guo, L. M. Moreno-Ramírez, J. Y. Law, Y. Zhang and V. Franco, Excellent cryogenic magnetocaloric properties in heavy rare-earth based HRENiGa$_2$ (HRE = Dy, Ho, or Er) compounds, *Sci. China Mater.*, 2023, **66**, 249–256.

9 Y. Zeng, F. Tian, T. Chang, K. Chen, S. Yang, K. Cao, C. Zhou and X. Song, Large magnetocaloric effect and near-zero thermal hysteresis in the rare earth intermetallic Tb$_{1-x}$Dy$_x$Co$_2$ compounds, *J. Phys.: Condens. Matter*, 2017, **29**, 055804.

10 A. Elouafi, S. Ezairi, F. Lmai and A. Tizliouine, Excellent magnetocaloric effect at cryogenic temperature in amorphous (Fe$_{35}$RE$_{65}$) (RE = Er, Dy and Gd) alloys, *J. Magn. Magn. Mater.*, 2023, **588**, 171381.

11 A. Herrero, I. R. Aseguinolaza, A. Oleaga, A. Garcia-Adeva, E. Apiñaniz, A. V. Garshev, V. O. Yapaskurt and A. V. Morozkin, Selecting optimal R$_6$TX$_2$ intermetallics (R = Gd, Tb, Dy; T = Mn, Fe, Co, Ni; X = Sb, Te) for magnetic refrigeration, *Dalton Trans.*, 2023, **52**, 5780–5797.

12 Y. Zhang, Y. Xie, J. Wei and W. Hao, Experimental and theoretical insights into the structural, magnetic, and low-temperature magnetocaloric properties of RE$_2$CoTiO$_6$ (RE = Gd, Dy, and Er) double perovskite oxides, *J. Mater. Chem. A*, 2024, **12**, 32396–32407.

13 F. Chen, Y. Na, Y. Xie and Y. Zhang, Insight into the Structural and Magnetic Properties of PrZnSi and NdZnSi Compounds Featuring Large Low-Temperature Magnetocaloric Effects, *ACS Appl. Mater. Interfaces*, 2024, **16**, 52719–52726.

14 A. Biswas, T. Del Rose, Y. Mudryk, P. O. Ribeiro, B. P. Alho, V. S. R. de Sousa, E. P. Nóbrega, P. J. von Rankc and V. K. Pecharsky, Hidden first-order phase transitions and large magnetocaloric effects in GdNi$_{1-x}$Co$_x$, *J. Alloys Compd.*, 2022, **897**, 163186.

15 I. R. Aseguinolaza, A. Herrero, A. J. Garcia-Adeva, E. Apiñaniz, A. V. Garshev, A. V. Morozkin and A. Oleaga, Broad table-like magnetocaloric effect in the full hydrogen liquefaction range in Gd$_3$Ni$_6$XY, *J. Alloys Compd.*, 2025, **1010**, 177154.

16 S. Sharma and P. Kumar, Modifications in the magnetocaloric effect owing to composition changes in Gd$_2$In$_{1-x}$Ge$_x$ ($0 \leq x \leq 0.2$) system of compounds, *AIP Adv.*, 2022, **12**, 035127.

17 S. Ghosh and S. Ghosh, Understanding the origin of the magnetocaloric effects in substitutional Ni-Mn-Sb-Z (Z = Fe, Co, Cu) compounds: Insights from first-principles calculations, *Phys. Rev. B*, 2020, **101**, 024109.

18 A. J. Garcia-Adeva, E. Apiñaniz, A. Herrero, I. R. Aseguinolaza and A. Oleaga, First-principle calculations of magnetic properties of Ho$_6$(Fe, Mn)Bi$_2$ compounds, *Rare Met.*, 2024, **43**, 6034–6047.

19 A. Herrero, A. Oleaga, A. Provino, I. R. Aseguinolaza, A. Salazar, D. Peddis and P. Manfrinetti, Crystallographic, magnetic and magnetocaloric properties in novel intermetallic materials R$_3$CoNi (R = Tb, Dy, Ho, Er, Tm, Lu), *J. Alloys Compd.*, 2021, **865**, 158948.

20 A. Oleaga, A. Erkoreka, A. Herrero, A. Provino, D. Peddis and P. Manfrinetti, Effect of Nd doping on the crystallographic, magnetic, and magnetocaloric properties of Nd$_x$Gd$_{3-x}$CoNi, *APL Mater.*, 2023, **11**, 061112.

21 C. Ritter, A. Provino, F. Fauth, S. K. Dhar, V. K. Pecharsky and P. Manfrinetti, From Tb$_3$Ni$_2$ to Tb$_3$CoNi: The interplay between chemistry, structure, and magnetism, *Phys. Rev. Mater.*, 2019, **3**, 024406.

22 A. Provino, V. Smetana, D. Paudyal, K. A. Gschneidner, Jr., A.-V. Mudring, V. K. Pecharsky, P. Manfrinetti and M. Putti, Gd$_3$Ni$_2$ and Gd$_3$Co$_x$Ni$_{2-x}$: Magnetism and unexpected Co/Ni crystallographic ordering, *J. Mater. Chem. C*, 2016, **4**, 6078–6089.

23 J. M. Moreau, D. Paccard and E. Parthé, The monoclinic, CrB-related, crystal structure of Tb$_3$Ni$_2$, Dy$_3$Ni$_2$ and Ho$_3$Ni$_2$, *Acta Crystallogr., Sect. B*, 1974, **30**, 2583–2586.

24 J. M. Moreau, E. Parthé and D. Paccard, The orthorhombic structure of Y$_3$Co$_2$, a shift structure variation of the monoclinic Dy$_3$Ni$_2$ type, *Acta Crystallogr., Sect. B*, 1975, **31**, 747–749.

25 P. Villars and K. Cenzual, *Pearson's Crystal Data: Crystal Structure Database for Inorganic Compounds (on DVD)*, Release 2022/23, ASM International, Materials Park, Ohio, USA.

26 A. Provino, V. K. Pecharsky, C. Bernini, V. Smetana, A.-V. Mudring and P. Manfrinetti, Solubility limits, magnetic and magnetocaloric properties of MoB-type GdCo$_x$Ni$_{1-x}$ ($0.47 \leq x \leq 0.72$)", *J. Alloys Compd.*, 2023, **948**, 169605.

27 K. Yvon, W. Jeitschko and E. Parthé, LAZY PULVERIX, a computer program, for calculating X-ray and neutron diffraction powder patterns, *J. Appl. Crystallogr.*, 1977, **10**, 73–74.

28 J. Rodriguez-Carvajal, Recent advances in magnetic structure determination by neutron powder diffraction, *Phys. B*, 1993, **192**, 55–69.

29 *Bruker, APEX5, V2023.9-2*, Bruker AXS Inc., Madison, WI, USA, 2023.

30 G. Sheldrick, SHELXT - Integrated space-group and crystal-structure determination, *Acta Crystallogr., Sect. A:Found. Adv.*, 2015, **71**, 3–8.

31 G. Sheldrick, "Crystal structure refinement with SHELXL", *Acta Crystallogr., Sect. C:Struct. Chem.*, 2015, **71**, 3–8.

32 H. Neves Bez, H. Yibole, A. Pathak, Y. Mudryk and V. K. Pecharsky, "Best practices in evaluation of the magnetocaloric effect from bulk magnetization measurements", *J. Magn. Magn. Mater.*, 2018, **458**, 301–309.

9040 | *J. Mater. Chem. C*, 2025, **13**, 9027–9041

This journal is © The Royal Society of Chemistry 2025

33 W. Jiang, X. Z. Zhou, G. Williams, Y. Mukovskii and K. Glazyrin, Griffiths phase and critical behavior in single-crystal $La_{0.7}$-$Ba_{0.3}MnO_3$: Phase diagram for $La_{1-x}Ba_xMnO_3$ ($x \leq 0.33$), *Phys. Rev. B:Condens. Matter Mater. Phys.*, 2008, **77**, 064424.

34 W. Jiang, X. Z. Zhou, G. Williams, Y. Mukovskii and K. Glazyrin, Critical behavior and transport properties of single crystal $Pr_{1-x}Ca_xMnO_3$ ($x = 0.27$, and 0.29), *Phys. Rev. B:Condens. Matter Mater. Phys.*, 2008, **78**, 144409.

35 E. Teatum, K. A. Gschneidner Jr. and J. Waber, Compilation of calculated data useful in predicting metallurgical behavior of the elements in binary alloy systems, Rep LA-4003, NTIS, Springfield, VA, 1968.

36 K. Momma and F. Izumi, VESTA 3 for three-dimensional visualization of crystal, volumetric and morphology data, *J. Appl. Crystallogr.*, 2011, **44**, 1272–1276.

37 P. Villars and J. L. C. Daams, Atomic-environment classification of the chemical elements, *J. Alloys Compd.*, 1993, **197**, 177–196.

38 H. E. Stanley, *Introduction to Phase Transitions and Critical Phenomena*, Oxford University Press, 1971.

39 J. M. Yeomans, *Statistical Mechanics of Phase Transitions*, Oxford Science Publications, 1992.

40 M. Campostrini, M. Hasenbusch, A. Pelissetto, P. Rossi and E. Vicari, Critical exponents and equation of state of the three-dimensional Heisenberg universality class, *Phys. Rev. B:Condens. Matter Mater. Phys.*, 2002, **65**, 144520.

41 M. Campostrini, A. Pelissetto, P. Rossi and E. Vicari, "25-th order high-temperature expansion results for three-dimensional Ising-like systems on the simple-cubic lattice", *Phys. Rev. E:Stat., Nonlinear, Soft Matter Phys.*, 2002, **65**, 066127.

42 B. K. Banerjee, "On a generalized approach to first and second-order magnetic transitions", *Phys. Lett.*, 1964, **12**, 16–17.

43 A. R. Chowdhury, G. S. Collins and C. Hohenemser, "Static universality class implied by the critical exponents of Gd", *Phys. Rev.*, 1986, **33**, 6231.

44 A. Herrero, A. Oleaga, P. Manfrinetti, A. Provino and A. Salazar, "Critical behavior of the ferromagnetic transition in GdSc(Si,Ge) intermetallic compounds", *Intermetallics*, 2018, **101**, 64–71.

45 A. Oleaga, A. Herrero, A. Salazar, A. V. Garshev, V. O. Yapaskurt and A. V. Morozkin, "Magnetocaloric properties and unconventional critical behavior in $(Gd,Tb)_6(Fe,Mn)Bi_2$ intermetallics", *J. Alloys Compd.*, 2020, **843**, 155937.

46 J. Y. Law, A. Diaz-Garcia, L. M. Moreno-Ramirez and V. Franco, "Increased magnetocaloric response of FeMnNi-GeSi high-entropy alloys", *Acta Mater.*, 2021, **212**, 116931.

47 J. Y. Law and V. Franco, "Review on magnetocaloric high-entropy alloys: Design and analysis methods", *J. Mater. Res.*, 2023, **38**, 37–51.

48 V. Franco, J. S. Blázquez, J. J. Ipus, J. Y. Law, L. M. Moreno-Ramírez and A. Conde, "Magnetocaloric effect: From materials research to refrigeration devices", *Prog. Mater. Sci.*, 2018, **93**, 112–232.

49 C. Romero-Muñiz, R. Tamura, S. Tanaka and V. Franco, "Applicability of scaling behavior and power laws in the analysis of the magnetocaloric effect in second-order phase transition materials", *Phys. Rev. B*, 2016, **94**, 134401.

50 V. Franco, A. Conde, J. M. Romero-Enrique and J. S. Blázquez, "A universal curve for the magnetocaloric effect: an analysis based on scaling relations", *J. Phys.: Condens. Matter*, 2008, **20**, 285207.

51 J. Y. Law, V. Franco, L. M. Moreno-Ramirez, A. Conde, D. Y. Karpenkov, I. Radulov, K. P. Skokov and O. Gutfleisch, "A quantitative criterion for determining the order of magnetic phase transitions using the magnetocaloric effect", *Nat. Commun.*, 2018, **9**, 2680.

52 V. Franco, J. S. Blázquez and A. Conde, "Field dependence of the magnetocaloric effect in materials with a second-order phase transition: A master curve for the magnetic entropy change", *Appl. Phys. Lett.*, 2006, **89**, 222512.

53 V. Franco and A. Conde, "Scaling laws for the magnetocaloric effect in second-order phase transitions: from physics to applications for the characterization of materials", *Int. J. Refrig.*, 2010, **33**, 465–473.

This journal is © The Royal Society of Chemistry 2025

J. Mater. Chem. C, 2025, **13**, 9027–9041 | **9041**